

Predissociation dynamics of the hydroxyl radical (OH) based on a five-state spectroscopic model

G. B. Mitev,¹ Jonathan Tennyson,¹ and Sergei N. Yurchenko¹

Department of Physics and Astronomy, University College London, Gower St, London WC1E 6BT, UK

(*Electronic mail: j.tennyson@ucl.ac.uk)

(*Electronic mail: georgi.mitev.16@ucl.ac.uk)

(Dated: 1 April 2024)

Multi-reference configuration interaction (MRCI) potential energy curves (PECs) and spin-orbit couplings for the X ²Π, A ²Σ⁺, 1 ²Σ⁻, 1 ⁴Σ⁻, and 1 ⁴Π states of OH are computed and refined against empirical energy levels and transitions to produce a spectroscopic model. Predissociation lifetimes are determined by discretising continuum states in the variational method nuclear motion calculation by restricting the calculation to finite range of internuclear separations. Varying this range give a series of avoided crossings between quasi-bound states associated with the A ²Σ⁺ and continuum states, from which predissociation lifetimes are extracted. 424 quasi-bound A ²Σ⁺ state rovibronic energy levels are analysed and 374 predissociation lifetimes are produced, offering good coverage of the predissociation region. Agreement with measured lifetimes is satisfactory and a majority of computed results were within experimental uncertainty. A previously unreported A ²Σ⁺ state predissociation channel which goes via the X ²Π is identified in the calculations. A python package, BINSLT, is produced to calculate predissociation lifetimes, associated line broadening parameters, and uncertainties from DUO *.states files is made available. The PECs and other curves from this work will be used to produce a rovibronic ExoMol linelist and temperature-dependent photodissociation cross sections for the hydroxyl radical.

I. INTRODUCTION

The hydroxyl radical OH is of significance in a diverse set of physical systems and as such has been extensively studied. OH is of high importance due to its presence in combustion, atmospheric and interstellar chemistry, and as a key constituent of the Earth's atmosphere¹⁻⁷. Furthermore, OH has been detected recently in the atmosphere of Ultra-hot Jupiters WASP-76b and WASP-33b^{8,9}. The many high resolution spectroscopy studies on OH have recently been comprehensively reviewed by Furtenbacher *et al.*¹⁰ as part of their MARVEL (measured active rotation energy level) study. The *ab initio* electronic structure and predissociation dynamics of OH have been of interest for many years. Much of the early theoretical work was done by Langhoff, van Dishoeck, Dalgarno, Bauschlicher and Wetmore¹¹⁻¹⁵, these works have seen extensive use in other theoretical studies¹⁶⁻²⁴. Further *ab initio* studies have been completed more recently with more computational power and larger basis sets^{16,25-28}. We particularly highlight the work of van der Loo and Groenenboom²⁵ which provided a starting point this study.

Despite the need for high-accuracy potential energy curves and coupling curves, the angular momentum coupling curves do not seem to have been reported. Angular momentum coupling corresponds to the Λ-doubling in the ground X ²Π electronic state energy levels²⁹ and are required for accurate modelling of the *e/f* parity splittings in both X ²Π and A ²Σ⁺ states. This splitting has been reported to be anomalously high at ultra-cold temperatures³⁰, hence, the angular momentum coupling between the X ²Π and first electronic excited

state, A ²Σ⁺ should also be of interest to ultra-cold physics experiments. The effect of predissociation of the A ²Σ⁺ energy levels caused by a spin-orbit interaction with repulsive (unbound) electronic states 1, ²Σ⁻, 1, ⁴Σ⁻ and 1, ⁴Π is investigated. Predissociation is one of the main sources of line broadening in the A–X rovibronic transitions, and has been extensively studied both experimentally and theoretically, for which lifetimes, line positions, line widths, rates, and branching ratios have been reported^{17-24,31-38}. A summary of available lifetimes data can be found is given below in Table IV. In the next section, details of the electronic structure calculations and spectroscopic model refinement procedure are presented. The method used to compute predissociation lifetime is based on use of variational bound-state nuclear-motion program DUO.³⁹ Section 3 discusses how DUO is used to study predissociation; a fuller discussion of this method will be presented in a paper⁴⁰ henceforth referred to as Paper I. Section V presents the final spectroscopic model and compares our calculated lifetimes with their literature counterparts. A summary of findings and proposed future work are presented in section VI.

II. METHODS: AB INITIO

The aim of this study is to produce a complete set of predissociation lifetimes for the A ²Σ⁺ state in the OH radical. An accurate spectroscopic model is needed to perform the lifetime calculations. To produce this model, a high level of theory was employed to calculate *ab initio* PECs and coupling curves for the X ²Π, A ²Σ⁺, and the dissociative 1 (²Σ⁻, ⁴Σ⁻, ⁴Π) states,

see Fig. 1. These are refined against experimental values in sec. III B.

A. *Ab initio* electronic structure calculations

The initial potential energy curves (PECs), spin-orbit coupling curves (SOCs) and angular momentum coupling curves (AMCs) were computed using the MOLPRO quantum chemistry program⁴¹⁻⁴³. Following van der Loo and Groenenboom²⁵, optimal molecular orbitals were computed using carefully selected combinations of state-averaged complete active space self-consistent field (SA-CASSCF)⁴⁴ calculations: details of which are given in Table I. These orbitals provide the input to multi-reference configuration interaction (MRCI) calculations which included a Davidson correction⁴⁵ to the energies. Final results were computed using an aug-cc-pV6Z basis set. The calculations were performed over internuclear distances ranging from 1 to 10 a_0 with a greater density of points around the equilibrium bond length. We ensured that no ${}^2\Delta$ states were obfuscating the presence of the desired ${}^2\Sigma^\pm$ states by calculating PECs for both A_1 and A_2 irreducible representations of C_{2v} , and selecting the appropriate symmetries. There are two linearly independent spin components in the ${}^4\Pi$ state giving rise to the same value of $|\Omega| = \frac{1}{2}$: $|1' {}^4\Pi\rangle \rightarrow \Lambda = -1, \Sigma = \frac{3}{2}$ and $|1 {}^4\Pi\rangle \rightarrow \Lambda = 1, \Sigma = -\frac{1}{2}$.

The spin-orbit coupling between the $A {}^2\Sigma^+$ and $1 {}^4\Pi$ states have the relationship,

$$\langle 1 {}^4\Pi | \hat{H}_{SO} | A {}^2\Sigma^+ \rangle = -\sqrt{3} \langle 1' {}^4\Pi | \hat{H}_{SO} | A {}^2\Sigma^+ \rangle \quad (1)$$

derived from the application of the Wigner-Eckart theorem^{16,28}. In DUO, for spin-orbit matrix elements it is sufficient to specify only one of these combinations with the correct Λ and Σ , the other is generated using the Wigner-Eckart theorem. Here we select $1 {}^4\Pi$, where $\Sigma = -\frac{1}{2}$, $\Lambda = 1$ as is done in Parlant and Yarkony²⁸. One should note it does not matter which coupling is chosen, as long as the correct Λ, Σ combination is given in Duo. MOLPRO produces coupling curves and dipoles with an arbitrary phase factor of ± 1 or $\pm i$ which is not guaranteed consistent between geometries. This uncertainty in phase leads to discontinuities in the curves and hence requires post-processing. Within an MRCI calculation informed by a set of SA-CASSCF orbitals, the phase may not be consistent between geometries, however it is consistent over all curves computed with those orbitals for a given geometry; any discontinuities will appear in the same places for all curves⁴⁶. The coupling curves in this study, however, were not all computed with one set of orbitals and instead were split up as shown in the SA-CASSCF column in Table I. Inter-SA-CASSCF phase consistency was ensured by first smoothing all curves with an arbitrary global phase and comparing to a set of reference curves. These were produced by performing an aug-cc-pVTZ calculation with all states present in the SA-CASSCF, ensuring phase consistency between all relevant curves. Visual representations of these curves can be seen in Figs. 1, 2, and 3

TABLE I. Summary of *ab initio* electronic structure calculation details. All calculations use aug-cc-pV6Z basis set with the first σ orbital closed. Orbitals correspond to the point group symmetry C_{2v} .

Curve	SA-CASSCF	Space
PECs		
$X {}^2\Pi$	$X {}^2\Pi_x, X {}^2\Pi_y$	$5\sigma 2\pi$
$A {}^2\Sigma^+, 1 {}^2\Sigma^-$	$A {}^2\Sigma^+, 1 {}^2\Sigma^-$	$5\sigma 2\pi$
$1 {}^4\Sigma^-$	$A {}^2\Sigma^+, 1 {}^2\Sigma^-, 1 {}^4\Sigma^-$	$5\sigma 2\pi$
$1 {}^4\Pi$	$1 {}^4\Pi_x, 1 {}^4\Pi_y, A {}^2\Sigma^+$	$6\sigma 2\pi$
Coupling Curves		
$\langle X {}^2\Pi \hat{H}_{SO} A {}^2\Sigma^+ \rangle$	$X {}^2\Pi_x, X {}^2\Pi_y, A {}^2\Sigma^+$	$5\sigma 2\pi$
$\langle X {}^2\Pi \hat{L}_x A {}^2\Sigma^+ \rangle$	$X {}^2\Pi_x, X {}^2\Pi_y, A {}^2\Sigma^+$	$5\sigma 2\pi$
$\langle X {}^2\Pi \hat{H}_{SO} X {}^2\Pi \rangle$	$X {}^2\Pi_x, X {}^2\Pi_y$	$5\sigma 2\pi$
$\langle A {}^2\Sigma^+ \hat{H}_{SO} 1 {}^2\Sigma^- \rangle$	$A {}^2\Sigma^+, 1 {}^2\Sigma^-$	$5\sigma 2\pi$
$\langle A {}^2\Sigma^+ \hat{H}_{SO} 1 {}^4\Sigma^- \rangle$	$A {}^2\Sigma^+, 1 {}^2\Sigma^-, 1 {}^4\Sigma^-$	$5\sigma 2\pi$
$\langle A {}^2\Sigma^+ \hat{H}_{SO} 1 {}^4\Pi \rangle$	$1 {}^4\Pi_x, 1 {}^4\Pi_y, A {}^2\Sigma^+$	$6\sigma 2\pi$

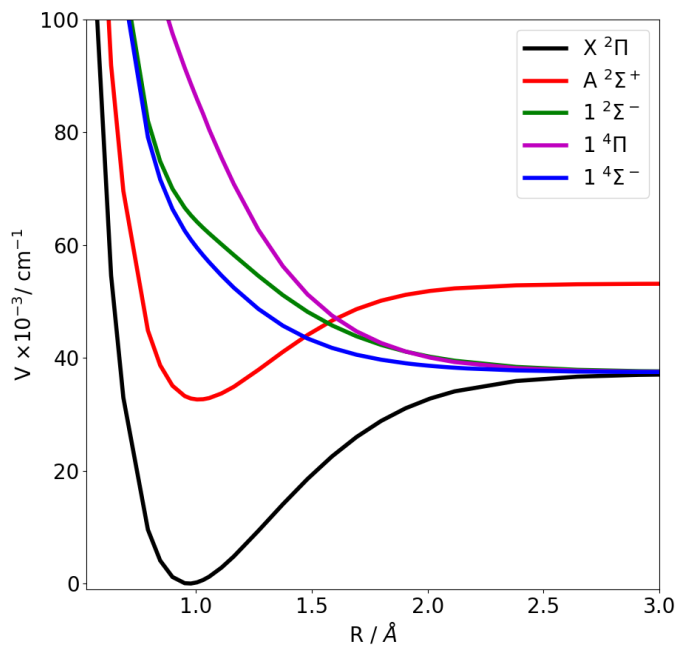


FIG. 1. *Ab initio* potential energy curves for OH as computed in MOLPRO.

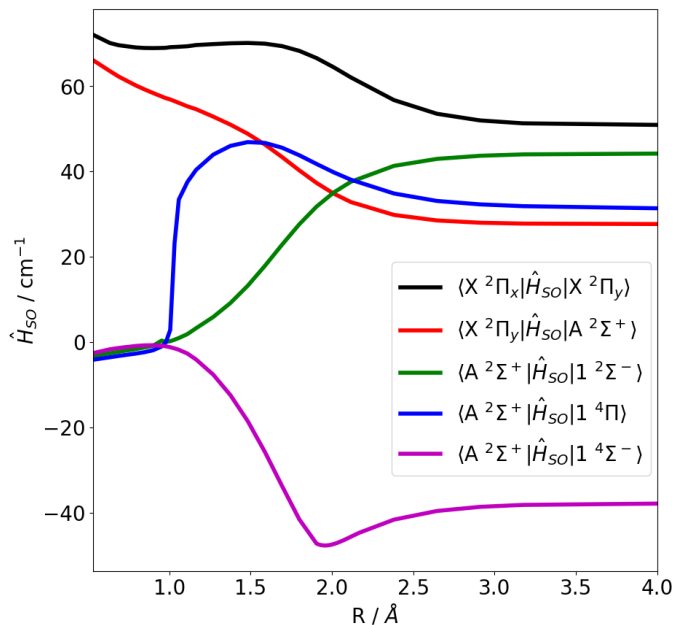


FIG. 2. Diagonal and off-diagonal *ab initio* spin-orbit coupling curves of OH as computed in MOLPRO. The curves here also have an associated factor of $\pm i$.

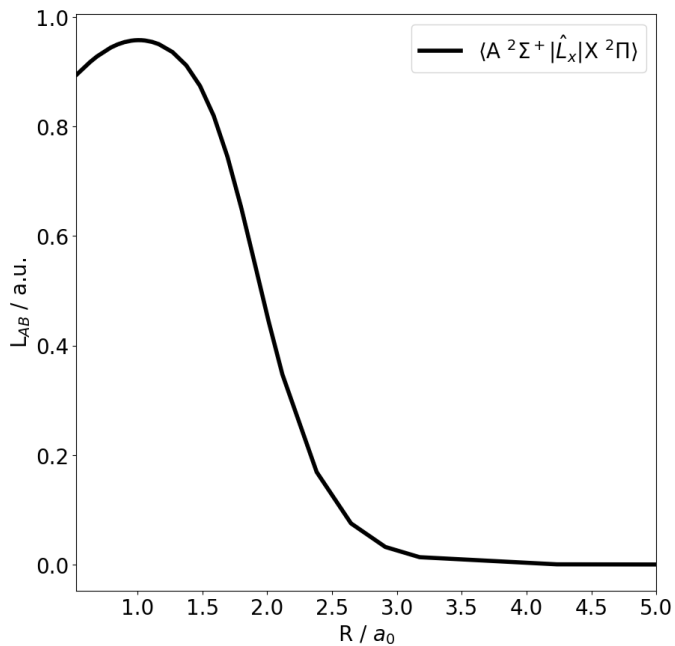


FIG. 3. *Ab initio* L-uncoupling matrix elements for OH as computed in MOLPRO. In the cartesian coordinate system, there is a factor of $\pm i$.

III. METHODS: HYDROXYL SPECTROSCOPIC MODEL

A. Global parameters

The curves produced above provide input to the nuclear motion code DUO⁴⁷, an open-source Fortran 2009 program which provides variational solutions to the coupled rovibronic Schrödinger equations for a general open-shell diatomic molecule. Rovibronic energy levels and transitions are evaluated for the mutually perturbed $X^2\Pi$ and $A^2\Sigma^+$ states. However, the *ab initio* curves are insufficient for accurate reproduction and extrapolation of energy levels for this system despite the high level of *ab initio* theory employed.

A number of global parameters need to be established before running a DUO calculation, they are as follows: The size of vibrational basis sets (v_{\max}) for each electronic state, the start (r_{\min}) and end (r_c) of the calculation box, the number of grid points, and the maximum value for J . These considerations are made to ensure converged solutions for the energy levels. The start and end of the box was set to 0.53 Å and 8 Å respectively with a grid size of 801 points. The density of rovibronic states increases with energy. States near the top end of the available vibrational basis are unstable as they are asymmetrically perturbed by local rovibronic states due to lack of states at $v > v_{\max}$ which means that an insufficiently large v_{\max} may lead to bound state solutions that may not be stable upon variation of the box size. v_{\max} was selected for each electronic state iteratively. By extracting energy eigenvalues within the relevant fitting region for increasing v_{\max} , we can set v_{\max} such that the energy levels are converged. This was found to occur when $v_{\max}^X \geq 110$ and $v_{\max}^A \geq 90$. The size of the vibrational basis sets were hence set to 110 and 90 for the $X^2\Pi$ and $A^2\Sigma^+$ states respectively. The maximum value for J , J_{\max} , was set to 50.5.

B. Fitting

The PECs and coupling curves were refined by making constrained adjustments to parameters which describe them with respect to a set of observed data, which can be either empirical energy levels or transitions. These data are supplied by the recent MARVEL data set¹⁰. Energy level coverage of this dataset is summarized in table II. Curve refinement is performed in DUO by least squares fitting to this data set. DUO provides three types of fitting one can use; variation of parameters that describe a curve (sec. III B 1), variation of parameters that describe a morphing function (*morphing*, see sec. III B 2), and direct variation of individual grid points. In each case the optimization is based on a non-linear conjugate gradient method⁴⁷ with respect to an empirical data set.

TABLE II. Coverage of MARVEL data set¹⁰ energy levels for the X $^2\Pi$ and A $^2\Sigma^+$ state of OH which have been used to refine *ab initio* PECs, SOCs and coupling constants for the production of a spectroscopic model.

v	J_{\min}	J_{\max}	Number of Levels
0	0.5	31.5	126
1	0.5	31.5	123
2	0.5	31.5	123
3	0.5	31.5	122
4	0.5	19.5	77
5	0.5	19.5	76
6	0.5	18.5	74
7	0.5	18.5	74
8	0.5	18.5	74
9	0.5	18.5	74
10	0.5	11.5	42
11	0.5	8.5	23
12	0.5	7.5	28
13	0.5	7.5	27
Total	0.5	31.5	1063
		A $^2\Sigma^+$	
0	0.5	31.5	64
1	0.5	28.5	58
2	0.5	19.5	40
3	0.5	26.5	54
4	0.5	19.5	40
5	0.5	7.5	15
6	0.5	8.5	17
7	0.5	7.5	16
8	0.5	9.5	19
9	0.5	8.5	17
Total	0.5	31.5	340
Grand Total			1403

1. Parameter variation fitting – pre-fitting

During parameter variation fitting, the curves must have some parametric form, and some initial set of parameters must be determined. For PECs, the form used in this study is the Extended Morse Oscillator (EMO)^{47,48}, given by

$$V_{\text{EMO}}(r) = T_e + (A_e - T_e) \left(1 - e^{-\beta(r)(r-r_e)}\right)^2 \quad (2)$$

where T_e is the potential minimum, $D_e = A_e - T_e$ is the dissociation energy relative to T_e , A_e is the dissociation asymptote, r_e is the equilibrium bond length, and $\beta(r)$ is a distance dependent exponent coefficient defined by the expansion term with coefficients β_i with respect to the reduced coordinate ξ_p , first introduced by Šurkus *et al.*⁴⁹ add are given by

$$\beta(r) = \sum_{i=0}^N \beta_i \xi_p^i; \quad N = \begin{cases} N_R & \text{for } r > r_e \\ N_L & \text{for } r \leq r_e \end{cases} \quad (3)$$

$$\xi_p(r) = \frac{r^p - r_e^p}{r^p + r_e^p}; \quad p = \begin{cases} p_R & \text{for } r > r_e \\ p_L & \text{for } r \leq r_e \end{cases} \quad (4)$$

This parametric form is flexible in that one can specify the behaviour around the equilibrium internuclear distance piecewise using the parameters N_L , N_R , p_L , and p_R , where $N_L \leq N_R$. The value of N_R hence defines the order of the expansion. This means one can establish a family of potential energy curves where the fundamental shape is determined by the set of parameters, S , where

$$S = \{p_L, p_R, N_L, N_R\}; \quad \{p_L, p_R, N_L, N_R\} \in \mathbb{Z}, \quad N_R \geq N_L. \quad (5)$$

For a given S , one can then find P which refines the shape to return appropriate energy levels, such that:

$$P = \{\beta_i, r_e, T_e, D_e\}; \quad i \leq N_R. \quad (6)$$

When fitting a PEC in DUO, S is fixed, and hence should be carefully chosen before optimizing P . Initial parameter selection has been performed by extending the method of Mitev *et al.*⁵⁰. Given that the elements of S are integers, one cannot use a standard optimization algorithm to optimize the values, and instead must solve the problem iteratively. The optimization of S is therefore initiated by establishing the set,

$$\sigma_S = \{S_0, \dots, S_n\} \quad (7)$$

$$\equiv \{\{p_{L_0}, p_{R_0}, N_{L_0}, N_{R_0}\}, \dots, \{p_{L_n}, p_{R_n}, N_{L_n}, N_{R_n}\}\} \quad (8)$$

which contains n elements of the set, S , as in Eq. (5) such that,

$$S_i \neq S_j \quad \forall i, j; \quad i \neq j. \quad (9)$$

This is the set of values of p_L , p_R , N_L , and N_R over which we would like to test. The test consists of, for each S_i , finding the conjugate P_i by least-squares fitting against the *ab initio* grid points in PYTHON (code available on [ExoMol GitHub](#)). In each case we find the reduced χ^2 test statistic, χ_v^2 and search for the S , P which return the lowest value. These parameters are then used as a starting point for fitting the PECs against experimental data in DUO. See table III for the σ_i parameters for the X $^2\Pi$ and A $^2\Sigma^+$ states in this study.

TABLE III. Parameters, σ_i which best describe *ab initio* PECs of OH as calculated in sec II A. Units in table footnote.

X $^2\Pi$		A $^2\Sigma^+$	
T_e	0	T_e	32612.251248000
r_e	0.970655035	r_e	1.013454000
A_e	37269.126195730	A_e	53204.256220000
p_L	4	p_L	3
p_R	3	p_R	3
N_L	6	N_L	4
N_R	8	N_R	8
β_0	2.292052187	β_0	2.620396000
β_1	-0.019995181	β_1	0.169768000
β_2	0.198099686	β_2	0.465289000
β_3	0.231459916	β_3	0.552208000
β_4	-0.136025012	β_4	0.413921000
β_5	-0.639517770	β_5	-5.174652000
β_6	-0.277770706	β_6	9.999998000
β_7	6.274892232	β_7	3.333865000
β_8	-4.898195146	β_8	-9.999764000

Units:

$$[T_e] = \text{cm}^{-1}$$

$$[A_e] = \text{cm}^{-1}$$

$$[r_e] = \text{\AA}$$

$$[\beta_i] = \text{\AA}^{-1}$$

2. Morphing

As discussed above, morphing is another available technique for model refinement. In this case, one does not vary the curve in question directly, but instead varies a morphing function, $f_m(r)$, which in turn, scales the *ab initio* curve, $f_{ai}(r)$ ^{51,52}:

$$f_{\text{morphed}}(r) = f_{\text{ai}}(r)f_m(r). \quad (10)$$

As was done in Mitev *et al.*⁵⁰, the *Polynomial decay* morphing function was used:

$$f_m(r) = \sum_{k=0}^N B_k z^k (1 - \xi_p) + \xi_p B_\infty, \quad (11)$$

where

$$z(r) = (r - r_{\text{ref}})e^{-\beta(r-r_{\text{ref}})^2 - \gamma(r-r_{\text{ref}})^4},$$

ξ_p is as in Eq. (4), B_k are variable expansion coefficients, β and γ are static coefficients typically set to 0.8 and 0.02 respectively, B_∞ is typically set to unity to preserve the asymptotic behaviour of f_{ai} , N is the order of expansion, and r_{ref} is the expansion center. r_{ref} is set to the equilibrium bond length of the lower energy electronic state. When fitting Eq. 11, only the B_k parameters are floated.

3. Constraining Curves

The asymptotic energy limit for all the curves in Fig. 1 was constrained by setting the value of D_e^X to the experimental value of D_0 from Joens⁵ with the added offset from the

zero-point energy of the X $^2\Pi$ state, E_0^X calculated in DUO, hence

$$D_e^X = D_0 + E_0^X. \quad (12)$$

The remaining curves' D_e where constrained with respect to D_e^X such that their respective atomic limit spacings match that of Kramida *et al.*⁵³.

C. MARVEL Data Set and Quantum Number Conventions

Furtenbacher *et al.*¹⁰ collected 15938 rovibronic transitions from 45 sources and produced values for 1624 empirical rovibronic energy levels for the system of electronic states, X $^2\Pi$, A $^2\Sigma^+$, B $^2\Sigma^+$, C $^2\Sigma^+$. 12413 and 1403 of these transitions and empirical energy levels respectively concern the X $^2\Pi$ and A $^2\Sigma^+$ states. Table II presents the coverage of the MARVEL energy levels used in this study.

The complete set of quantum numbers used to characterise the MARVEL energy levels are the state label (X $^2\Pi$, A $^2\Sigma^+$, $1^2\Sigma^-$, ...) total angular momentum, J , the vibrational quantum number, v , the rotationless parity, e/f and the projection of the total angular momentum on the molecular axis, $\Omega = \Sigma + \Lambda$, where, Σ and Λ are projections of the spin and orbital angular momenta on the molecular axis, respectively.

In line with the Hund's case (a) conventions used in DUO, the following quantum numbers are used to characterize the rovibronic states, $|J, v, \tau, \Sigma, \Lambda, \Omega, \text{State}\rangle$ where *State* is a counting number associated with the electronic states as ordered by potential minima, T_e and τ is the state parity $+/-$ (see Tenynson *et al.*²⁹ for conversion between e/f and τ), which can be directly related to the MARVEL data set.

Instead of using the the Hund's case (a) convention, many data sets on the rovibronic state of OH in the literature opt for the rotational quantum number N and the fine structure components, F_1 and F_2 (Hund's case (b)). In order to correlate these data with our MARVEL data set, their representations have been converted to the rigorous quantum labels J , e/f using the following relations.

For the A $^2\Sigma^+$ state:

$$J = \begin{cases} N + \frac{1}{2} & \text{for } F_1 \\ N - \frac{1}{2} & \text{for } F_2 \end{cases} \quad (13)$$

$$e/f = \begin{cases} f & \text{for } F_1 \\ e & \text{for } F_2 \end{cases} \quad (14)$$

These relations arise, in particular, as the A $^2\Sigma^+$ state levels are generally presented using Hund's case (b), hence the relation between J and N , Eq. (13) and due to the common approximation,

$$E_{F_1} = BN(N+1) + \frac{1}{2}\gamma N \quad (15)$$

$$E_{F_2} = BN(N+1) - \frac{1}{2}\gamma(N+1). \quad (16)$$

Therefore, because $\gamma \ll B$,⁷ where B is the rotational constant and γ is the spin-rotation constant,

$$E_{F_1} > E_{F_2} \quad \forall N, J \quad (17)$$

and since the $A^2\Sigma^+$ state has only parity splitting as $\Lambda^A = 0$, the F_1 and F_2 components correspond directly to f and e parities respectively (see Herzberg⁵⁴).

For the $X^2\Pi$ state the relevant Hund's case (a) approximation is:

$$E_{F_1} = B[(J+S)^2 - \Lambda^2] - \frac{1}{2}(A - 2B) \quad (18)$$

$$E_{F_2} = B[(J+S)^2 - \Lambda^2] + \frac{1}{2}(A - 2B) \quad (19)$$

Where A is the diagonal spin-orbit coupling. This is applied for a given parity and correlates with the following relation⁵⁴:

$$E_{F_1} = E(\Omega = \frac{3}{2}) \quad (20)$$

$$E_{F_2} = E(\Omega = \frac{1}{2}) \quad (21)$$

The quantum number correlations for the quartet $1(4\Sigma^-, 4\Pi)$ states have not been considered here as there are no experimental data which will require transformation.

IV. METHODS: PREDISSOCIATION LIFETIMES

OH predissociation lifetimes have long been the subject of theoretical and experimental studies, a summary of the available literature data has been provided in Table IV. The data provided by Heard *et al.*³⁴, Spaanjaars *et al.*³⁵ are given as predissociation rates and these have been inverted to return the required predissociation lifetimes. Brzozowski *et al.*³² provides measurements of the total lifetime which is given by

$$\tau = \frac{\tau_r \tau_p}{\tau_r + \tau_p} \quad (22)$$

where τ_r and τ_p are the radiative and predissociative lifetimes respectively. As these values include also the radiative lifetime, we expect our calculations to be greater than these values. This is compounded by the fact that the predissociation in the region of $v \in [0, 1, 2]$ is less dominant than in $v \geq 3$.

A novel method for the calculation of predissociation lifetimes is applied in this section. The full details of the method will be available in Paper I, however, a brief summary of the method is given below.

1. Energy resonances

An excited rovibronic state from $A^2\Sigma^+$ can predissociate via a spin-orbit interaction with a local repulsive state inducing the decay^{17,20,28,36,37}.

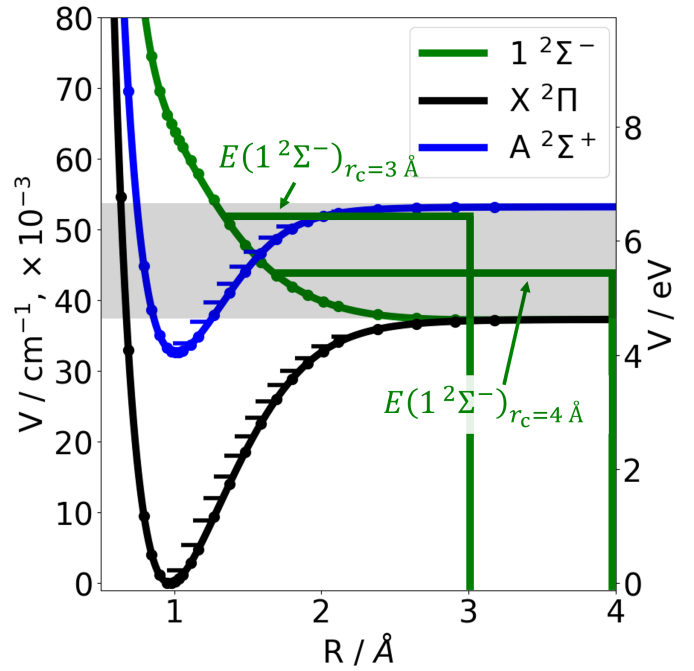


FIG. 4. A toy model of OH consisting of the $X^2\Pi$, $A^2\Sigma^+$, and $1^2\Sigma^-$ electronic states. The two green levels, $E(1^2\Sigma^-)_{r_c=3,4 \text{ \AA}}$ are continuum levels in the $1^2\Sigma^-$ electronic state with the same quantum numbers, however with different right-side box limits, r_c . This highlights the box size dependence of repulsive state energy levels. The shaded region covers energy levels between D_c^X and D_c^A .

In Fig. 4, the two green horizontal lines illustrate unbound state energy levels retrieved from DUO calculations with different right-side box limits, r_c . Both sets of calculations are performed with the same left-side box limit r_{\min} . By construction the nuclear motion wavefunctions are only finite between r_c and r_{\min} . The two green unbound state energy levels have the same quantum numbers $J, v, \tau, \Sigma, \Lambda, \Omega$, however, $E_{r_c=3 \text{ \AA}}$ returns a higher term value than $E_{r_c=4 \text{ \AA}}$. This is akin to the particle in a box, where increasing the size of the box compresses the distribution of energy levels closer to zero. Repeated calculations over varying r_c in DUO for iso-numeric continuum energy levels exhibits a relationship where the term values decrease with r_c , this is referred to as the *energy profile* of the continuum energy level.

The spin-orbit interaction between the $1^2\Sigma^-$ and $A^2\Sigma^+$ states, $\langle 2\Sigma^- | \xi | 2\Sigma^+ \rangle$, hence displaces the $A^2\Sigma^+$ state levels, which would otherwise be stable under variation of r_c . This *induced energy profile*, allows us to study the predissociation characteristics of the quasi-bound $A^2\Sigma^+$ state levels.

The energy levels of interest for this study are found in the shaded region of Fig. 4. This covers 424 rovibronic energy levels in the $A^2\Sigma^+$ state.

The quantum number coverage for the relevant energy levels is presented in Table V. Being above the first dissociation channel (D_c^X), each of these levels is quasi-bound and metastable with an associated characteristic lifetime, which we

TABLE IV. Summary of predissociation lifetime data available from experimental and theoretical sources.

Reference ^a	Lifetime (ps)		ν		J		Number of Lifetimes	Data Type
	Min	Max	Min	Max	Min	Max		
Experiment								
05DePoDe ³¹	17	23	4	4	0.5	7.5	8	Predissociation Lifetimes
21SuZhZh ³⁶	14	130000	2	4	0.5	2.5	2	Predissociation Lifetimes
78BrErLy ³²	33000	1110000	0	2	0.5	29.5	118	Total Lifetimes
91GrFa ³³	73	500	3	3	0.5	9.5	17	Predissociation Lifetimes
92HeCrJe ³⁴	62.89	312.50	3	3	0.5	13.5	27	Predissociation Rates
97SpMeMe ³⁵	29	167	3	3	4.5	14.5	20	Predissociation Rates
Theory								
80SiBaLe ³⁸	2.95	428.16	3	9	Not J Resolved		7	Predissociation Lifetimes
94KaSa ¹⁸	3.32	6895.10	1	7	Not J Resolved		7	Predissociation Lifetimes
99PaYa ²⁸	6000	9666000	0	4	0.5	30.5	107	Predissociation Lifetimes
Grand Total							313	
This work	2.1	3600000	0	9	0.5	35.5	374	Predissociation Lifetimes

^a Reference tags are given as YYAaBbCc, where YY is the last two digits of the publication year, AaBbCc are first two letters of (up to) first three authors surnames in order of appearance.

TABLE V. Quantum number coverage for quasi-bound A $^2\Sigma^+$ state rovibronic levels.

ν	J_{\min}	J_{\max}	Number of Levels	Number of Lifetimes ^a
0	13.5	35.5	44	21
1	2.5	33.5	62	35
2	0.5	31.5	63	63
3	0.5	28.5	57	57
4	0.5	25.5	51	51
5	0.5	22.5	45	45
6	0.5	19.5	39	39
7	0.5	15.5	31	31
8	0.5	11.5	23	23
9	0.5	4.5	9	9
Total			424	374

^a Number of levels for which a lifetime calculation is meaningful.

compute here. As discussed below, not all levels in the range had calculable predissociation lifetimes as per the method in Paper I, especially for levels with energy close to D_e^X .

Since repulsive electronic states have an infinitely dense set of continuum states, the position of the predissociating state, $|A^2\Sigma^+, Q\rangle$, where Q is the complete set of quantum numbers, $\{J, \nu, \tau\}$, has an uncertainty in the energy caused by the Pauli exclusion principle. This infinite set of states cannot be recovered using bound state methods for solving the Schrödinger equation for $r_c \rightarrow \infty$, such as used by DUO, although more expensive scattering methods can be employed using DUO just for the inner region⁵⁵.

Here we approximate the continuum behaviour by discretizing the continuum⁵⁶ and adapting the stabilization method^{57–59} to characterize the quasi-bound states. In this method, infinite potential walls are assumed at the box limits r_{\min} and r_c , leading to bound-like rovibronic solutions even for continuum or quasi-bound states. By changing the position of the right-side wall r_c , different continuum state term values can be gener-

ated and the uncertainty of the position of the quasi-bound states can be quantified as follows.

For a given box size defined by $r_c - r_{\min}$ with a infinite potential wall, one can compute the term values $\tilde{E}_{|A, Q\rangle}|_{r_c}$ of the given set of quasi-bound, meta-stable states $\{|A^2\Sigma^+, Q\rangle\}$. By varying r_c , one can then establish a dependence of $E_{|A, Q\rangle}$ on r_c . In this study, r_c was varied between $r_c = 8$ and 8.999 Å with the uniform spacing of 999 values ($\delta r_c = 0.001$ Å). This was done by repeating the DUO calculations while varying the right-side limit, r_c (see Sec. III A) and extracting the eigenenergies at each step. The number of the DUO sinc-DVR⁶⁰ grid points was increased as the box size was increased to maintain a uniform grid. Out of 999 runs, about 20 calculations failed, but these were simply ignored.

Figures 5 and 6 illustrate the box-size dependence for two A $^2\Sigma^+$ quasi-bound states of OH, $|A^2\Sigma^+, J = 0.5, \nu = 4, e\rangle$ and $|A^2\Sigma^+, J = 0.5, \nu = 2, e\rangle$ showing their ‘stabilisation’ character. The behavior is seen to be periodic with discontinuities at visually regular intervals and a central energy region in the middle. The typical resonance-like shapes are due to the interactions with continuum states. The discontinuities occur at the geometries where a crossing continuum energy level goes from pushing the quasi-bound level down to pushing it up and provide the energy level resonances from which we can calculate lifetimes. The line broadening parameter, Γ and hence the lifetime of the state, $\tau \propto 1/\Gamma$, are associated with the widths of these resonances.

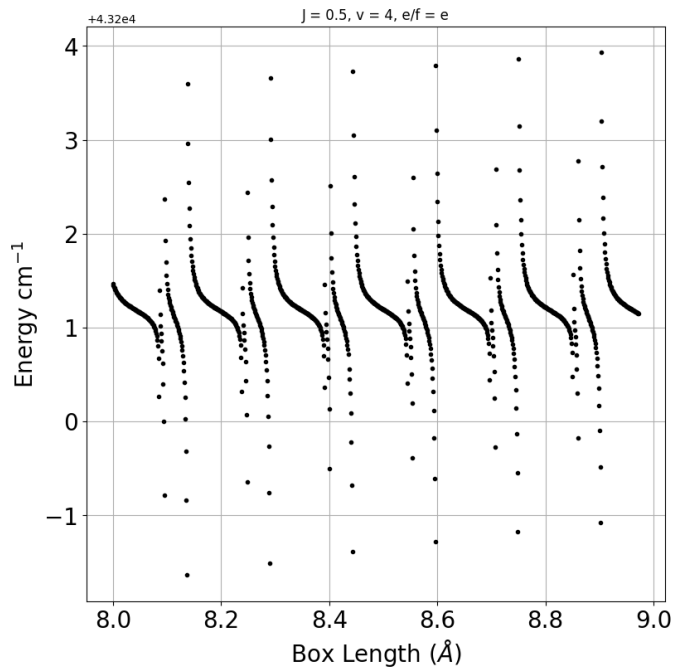


FIG. 5. The term value of the $|A^2\Sigma^+, J = 0.5, v = 4, e\rangle$ state as a function of the box length of the calculation in DUO, the variation of the energy is induced by crossings with energy levels in the repulsive states $1^2\Sigma^-, 1^4\Sigma^-,$ and $1^4\Pi$.

The interaction between $A^2\Sigma^+$ and the three continuum states $1^2\Sigma^-, 1^4\Sigma^-, 1^4\Pi$ are through the corresponding spin-orbit couplings from Fig. 2. There are several structures visible in Fig. 5, the asymptotes with the large wings and the asymptotes with the small wings. These substructures are caused by spin-orbit interactions with different electronic states, $1^2\Sigma^-, 1^4\Sigma^-,$ or $1^4\Pi$. The individual contributions can be resolved by performing calculations with only one of the three repulsive states and associated spin-orbit couplings present at a time, as illustrated in Fig. 6 for the $|A^2\Sigma^+, J = 0.5, v = 2, e\rangle$ state (this state has been chosen for its simplicity). It shows that all three states contribute to the minor asymptotic wings but only the $1^4\Sigma^-$ state corresponds to the major wings. This makes the $1^4\Sigma^-$ state a bigger contributor to the predissociative decay for this particular state (due to a greater effect on the overall broadening), which is corroborated by the branching ratios reported by Li and Zhang³⁷ who show that the $1^4\Sigma^-$ state is the primary branch.

For energy levels above D_e^X , $X^2\Pi$ state rovibronic levels become unbound and contribute to the perturbation of the $A^2\Sigma^+$ state level energies and hence provide an additional avenue for predissociation through the ground electronic state, see Fig. 7. The effect of predissociation through the $X^2\Pi$ state is small, and does not appear to have previously been reported. This effect cannot be isolated in our calculations, however, as removing the spin-orbit coupling between the $X^2\Pi$ and the $A^2\Sigma^+$ states shifts the energy levels too strongly (hundreds of cm^{-1}) to be comparable.

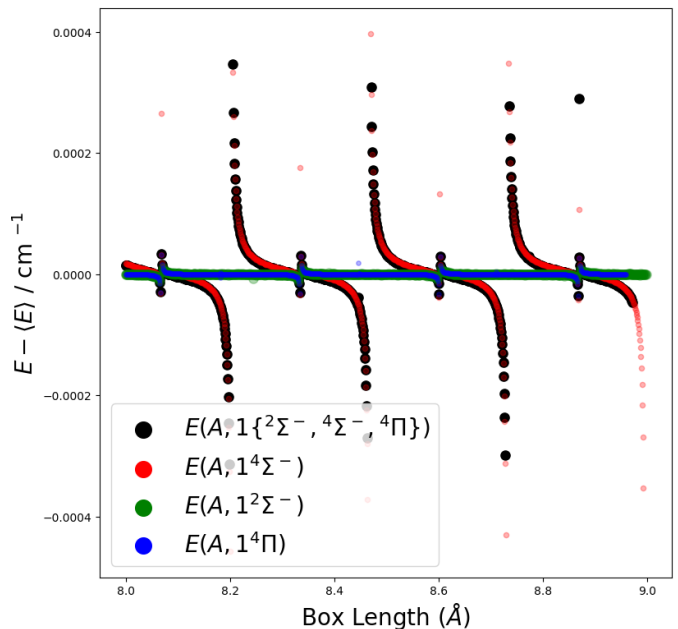


FIG. 6. Term value of the $|A^2\Sigma^+, J = 0.5, v = 2, e\rangle$ state as a function of the box length of the calculation in DUO. The different colors correspond to different spin-orbit contributions.

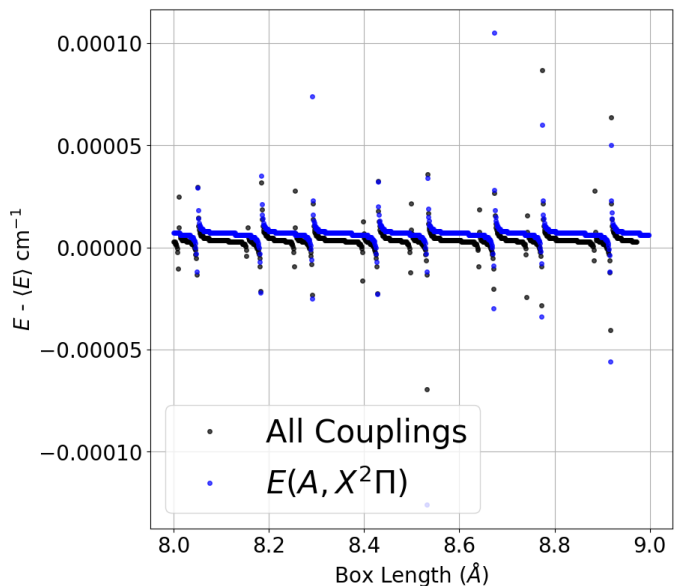


FIG. 7. Term value of the $|A^2\Sigma^+, J = 13.5, v = 1, f\rangle$ state as a function of the box length for a DUO calculation including the $X^2\Pi$ and $A^2\Sigma^+$ states only. The blue markers represent a shift in energy induced by the spin-orbit coupling between the $X^2\Pi$ and $A^2\Sigma^+$ states on the $A^2\Sigma^+$ state level.

2. Statistical treatment

To calculate the predissociation lifetime from the above results, one calculates the integral normalised histogram of the

energy data points centered around the mean ($E - \langle E \rangle$), see Fig. 8 for an example. The binning of the histogram and the training of the Lorentzian parameters is non-trivial and is discussed in Paper I.

The probability function describing the system's energy profile has the Lorentzian distribution¹⁹:

$$L(\tilde{E}; \tilde{E}_0, \Gamma) = \frac{\frac{1}{\pi}(\frac{1}{2}\Gamma)}{(\tilde{E} - \tilde{E}_0)^2 + (\frac{1}{2}\Gamma)^2} \quad (23)$$

where \tilde{E}_0 is the peak position of the Lorentzian and Γ is the full-width at half-maximum (line broadening parameter, in cm^{-1}). The parameters $\{\tilde{E}_0, \Gamma\}$ can be trained to best represent the histogram in Fig. 8, then the parameter Γ is inverted via the relationship

$$\tau_p = \frac{1}{2\pi c\Gamma} \quad (24)$$

where c is the speed of light in cm s^{-1} .

There is an associated uncertainty to the fitting of the Lorentzian profile and this is discussed in Sec. IV 3. The PYTHON package, BINSLT was written to perform these calculations; it is available for download from <https://github.com/exomol>.

A visualisation of the Lorentzian-distributed energy histogram is shown in Fig. 8, where it is superimposed with the corresponding induced energy profile for the $|A^2\Sigma^+, J = 0.5, v = 4, e\rangle$ state.

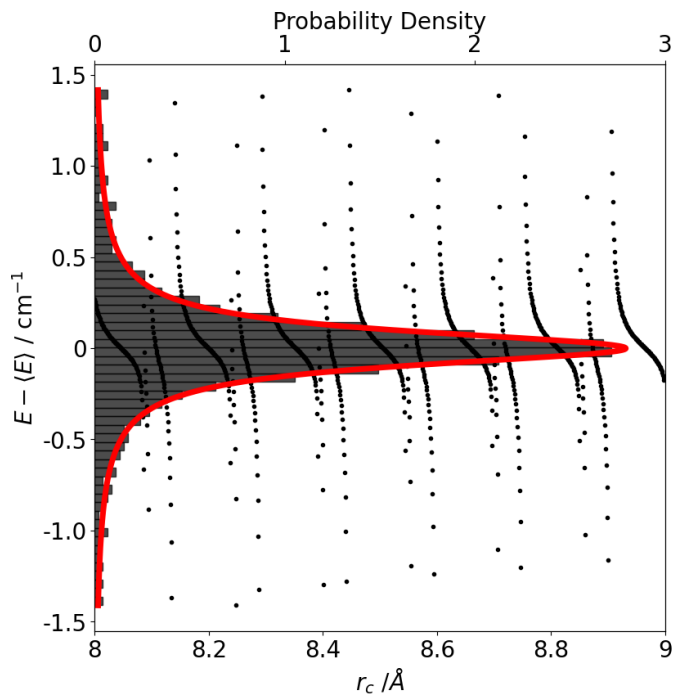


FIG. 8. Plot of the energy against box length with the fitted histogram of energy points for the $|A^2\Sigma^+, J = 0.5, v = 4, e\rangle$ state.

3. Uncertainty Estimation

The largest uncertainties arise in states with long predissociation lifetimes. Here we will consider only the lifetimes which are shorter than the radiative lifetimes. As discussed in Paper I, the uncertainty is made up for four components, which are assumed independent and systematic and so are added to produce a final uncertainty Δ_τ

$$\Delta_\tau = \Delta_M + \Delta_R + \Delta_B + \Delta_C, \quad (25)$$

where Δ_M is the uncertainty from convergence which is defined as $1 - M$ where M is the convergence level of the lifetime for a given state. This is typically the largest uncertainty and in cases of long lifetimes ($\tau_p > 10^5$ ps) this can be as high as 20%. For lifetimes between 10^4 and 10^5 ps, Δ_M is evaluated at 10% and for lifetimes shorter than 10^4 ps, this is found to be 5%.

Δ_R and Δ_B is the uncertainty from the positions of the repulsive and bound states' energy levels. Δ_B is very difficult to measure directly, as it requires that the energy level positions of the bound states can be controlled with high precision in order to establish a relationship between the energy offset and the lifetime. This is, at the moment, infeasible. This has been estimated, however, by probing the effect the repulsive energy level positions have on the lifetimes. The asymptotic energy of the continuum states go to the $O(^3P)$ level, the same as the $X^2\Pi$ state. $D_e(X)$ has been experimentally measured to an uncertainty of 10 cm^{-1} by Joens⁵ (see sec. III B 3). Our continuum curves were shifted down by 20 cm^{-1} and the lifetimes for the predissociative states with $J \in [0.5, 1.5]$ were re-computed and compared to the original model. This gives a conservative estimate on the uncertainty due to the position of the continuum curves, Δ_R of about 5%. The $A^2\Sigma^+$ state energy level position induced uncertainty, Δ_B is hence also estimated at 5%

Δ_C is the uncertainty of the numerical procedure excluding the problem of convergence. This is evaluated *in situ* for each state and has an average value over all states of approximately 2% in the case of OH. These uncertainties are distributed exponentially as is seen in Fig. 9.

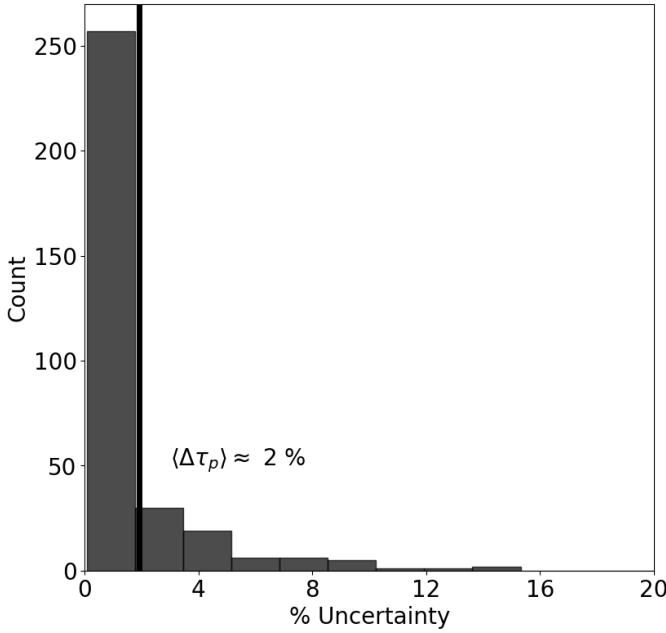


FIG. 9. Distribution of percentage uncertainties in the lifetime induced by the computational procedure.

The lifetimes supplied in the supplementary material have been fully treated as in the methods described above and more completely, in Paper I. Tab. VI gives a summary of the average uncertainties over different ranges of lifetimes in ps.

TABLE VI. Rules for attributing uncertainties for predissociation lifetimes calculated using the stabilization method for OH

Quantity	Value		
Lifetime range / ps	$[0, 10^4]$	$[10^4, 10^5]$	$[10^5, 10^7]$
Average Uncertainty / %	$15+\Delta_C$	$20+\Delta_C$	$30+\Delta_C$

V. RESULTS

A. Spectroscopic model parameters

Refinement of the curves representing the coupled model of the two states $X^2\Pi$ and $A^2\Sigma^+$ in DUO was performed by floating the parameters $r_e(X, A)$, $T_e(A)$, $\beta_i(X, A)$ (PECs) and B_k (spin-orbit and L-uncoupling curves)

Couplings to higher electronic states have not been considered for sake of simplicity in the model. Furthermore, couplings to repulsive electronic states for refinement of bound state energy levels have not been considered either. This has been done due to computational limitations as the box size of the calculation becomes an independent variable for the energy levels, see discussions above.

Along with the adjusted PECs and the *morphed* coupling curves, three more *empirical*, diagonal curves have been introduced to account for the aforementioned missing couplings²⁹.

These are the spin-rotation, $\gamma(X, A)$, the Λ -doubling $\alpha_{p2q}(X)$ and $q(X)$ ⁶¹, and the Born-Oppenheimer breakdown (BOB) radial property function⁶². The inclusion of such factors was necessary to refine the energy level reproduction without requiring the introduction of further electronic states or off-diagonal couplings. The Šurkus polynomial expansion function, $C(r)$ (see Eq. (26)), has been used as the parametric representation⁶³,

$$C(r) = T_e + (1 - \xi_p) \sum_{i \geq 0} B_i \xi_p^i + \xi_p B_\infty \quad (26)$$

where ξ_p is the reduced coordinate in Eq. (4). The parameters B_i and B_∞ are floated.

The dissociation limits, $D_e(X, A)$ were fixed to the values $D_e = D_0 + \text{ZPE}$, where the zero point energy of the ground state was extracted from the DUO calculation and found to be $\sim 1918 \text{ cm}^{-1}$, $D_0(X)$ was measured by Joens⁵ to $\pm 10 \text{ cm}^{-1}$, $D_e = D_0 + \text{ZPE}$, while $D_e(A)$ was estimated by adding the difference in energy between the $O(^3P)$ and $O(^1D)$ atomic levels using values from the NIST Online Database⁵³.

In DUO, one can fit spectroscopic model both against data sets of energy levels and of transitions in DUO. The process taken in this work was to fit it against the experimentally derived (MARVEL) energy levels by Furtenbacher *et al.*¹⁰.

A summary of fitted parameters is available in Tables VII, VIII, IX and a summary of uncertainties and RMS values is available in table X. The DUO input file is given in the supplementary information.

TABLE VII. Summary of the PEC parameters obtained from least squares fitting the $X^2\Pi$ and $A^2\Sigma^+$ states of OH to MARVEL energy levels from Furtenbacher *et al.*¹⁰ in Duo⁴⁷. All the figures are kept for the sake of preserving accuracy and reproducibility.

Parameter	$X^2\Pi$	$A^2\Sigma^+$
T_e	0	32663.976309068300
r_e	0.970020962666	1.005285998312
A_e	37501.792600000000	53369.654600000000
p_L	4	3
p_L	3	3
N_L	6	4
N_R	9	8
β_0	2.287411349533	2.625193503966
β_1	-0.008481205971	0.137874402944
β_2	0.138199166549	0.280685923916
β_3	-0.066491288959	0.687146152607
β_4	0.249817374269	1.374869049258
β_5	1.855331479551	-2.136036385410
β_6	2.083877071440	-14.858091727498
β_7	-21.177505781638	45.312091462135
β_8	34.392719961367	-32.477114187491
β_9	-16.859334102231	

TABLE VIII. Summary of the *morphing* parameters obtained from least squares fitting the X $^2\Pi$ and A $^2\Sigma^+$ states of OH to MARVEL energy levels and transitions from Furtenbacher *et al.*¹⁰ in Duo⁴⁷.

Parameter	ξ_X	ξ_{XA}	L_{XA}
r_e	0.970655034638	0.970655034638	0.9704443874981
β	0.8	0.8	0.8
γ	0.02	0.02	0.02
p	6	6	2
B_0	1.008496273609	0.675170320954	0.772527250694
B_1	-0.504517931107	-0.799178556532	-0.649959182912
B_2	0.127429582028	-2.036097977961	-0.712564567820
B_∞	1.000000000	1.000000000	1.000000000

TABLE X. Summary of the energy RMS values, in cm^{-1} , obtained from least squares fitting the X $^2\Pi$ and A $^2\Sigma^+$ states of OH to MARVEL transitions from Furtenbacher *et al.*¹⁰ in Duo⁴⁷

v	RMS_X	RMS_A
0	0.08	0.07
1	0.09	0.19
2	0.15	1.05
3	0.08	0.76
4	0.12	0.61
5	0.06	1.96
6	0.11	3.23
7	0.14	4.70
8	0.08	1.64
9	0.25	4.58
10	0.25	
11	0.70	
12	1.34	
13	1.13	
Whole State	0.33	1.79

B. Predissociation lifetimes

BINSLT was used to compute the predissociation lifetimes of 374 quasi-bound A $^2\Sigma^+$ rovibronic states with follow up processing completed as further described in Paper I. 50 out of the allowed 424 states could not be processed as their energy profiles were too narrow and had insufficient resolution to compute Γ_p .

A comparison with the lifetimes available in the literature (experiment and theory) and this work is illustrated in Fig. 10, where the lifetime values are plotted as a function of J . The corresponding J -averaged percentage errors and their standard deviations are given in Table XI. A full tabulation of these data is available in the supplementary material for reference.

Table XI shows that there is a satisfactory agreement between the lifetimes presented here and experiment; there is particularly good agreement for the cases where $v = 3, 4$, see Fig. 10. In these cases, most results agreed within uncertainty (51/73 cases) and in regions where they did not agree, the mean percentage real difference in this region is 15%. The percentage

real difference, ${}^R\Delta\%$ and percentage difference, $\Delta\%$ here is defined as

$$D = \frac{|\Delta| - (\delta_{\text{calc}} + \delta_{\text{lit}})}{\tau_{\text{lit}}} \quad (27)$$

$${}^R\Delta\% = \begin{cases} D & \text{for } D > 0 \\ 0 & \text{otherwise} \end{cases} \quad (28)$$

$$\Delta\% = \frac{\tau_{\text{lit}} - \tau_{\text{calc}}}{\tau_{\text{lit}}} \equiv \frac{\Delta}{\tau_{\text{lit}}}, \quad (29)$$

where $\tau_{\text{lit,calc}}$ are the literature and calculated predissociation lifetimes respectively, Δ is the difference in those values, and $\delta_{\text{lit,calc}}$ are the uncertainties quoted in the literature and calculated values respectively.

The noticeable exceptions to this are the lifetimes for $v \in [0, 1, 2]$ from Brzozowski *et al.*³². The experimental values in question here are total lifetimes rather than predissociation lifetimes. For $v < 2$, radiative decay is the dominant source of broadening, hence the lifetimes of Brzozowski *et al.*³² measurements should underestimate the predissociation lifetime. For $v = 2$, predissociation is dominant, however radiative decay appears to be significant in the low J region (< 6.5).

One can consider the individual widths of the radiative and predissociative components, $\Gamma_{r,p}$ and that the total width is $\Gamma = \Gamma_r + \Gamma_p$ and extract the dominance of the radiative decay, R_D such that

$$R_D = \frac{\Gamma_r}{\Gamma} \quad (30)$$

From our calculations, we compute R_D and estimate the predissociation lifetime of Brzozowski *et al.*³² through the relation

$$\tau_p = \frac{\tau}{1 - R_D} \quad (31)$$

and from this we are able to recover agreement within uncertainty with Brzozowski *et al.*³².

TABLE IX. Summary of the empirical parameters obtained from least squares fitting the X $^2\Pi$ and A $^2\Sigma^+$ states of OH to MARVEL energy levels and transitions from Furtenbacher *et al.*¹⁰ in Duo⁴⁷

	BOB(A $^2\Sigma^+$)		γ_X	γ_A	α_{p2q}	q
r_e (Å)	0.969785542585	0.969785542585	0.969785542585	0.969785542585	0.969785542585	0.969785542585
p	2	2	2	2	2	2
N	3	3	3	3	3	3
B_0 (Å $^{-1}$)	-0.013387427200	-0.082615835520	0.107579056717	0.081298271720	-0.015657399328	
B_∞ (Å $^{-1}$)	-0.000897768443	0.029822159900	0.019259293154	-0.116865046681	0.016057094058	

TABLE XI. Summary of comparison between predissociation lifetimes as calculated in this work and available literature values. Differences are averaged over J for a given v . Only rotationally resolved literature lifetimes are compared here (see Table IV). Full comparison dataset provided in supplementary data.

Type	Ref	v	$\langle\Delta\% \rangle$	Number	C_A	$\langle^R\Delta\% \rangle$	
Exp	05DePoDe ³¹	4	-0.2	8	8	0.0	
	21SuZhZh ³⁶	2	-70.0	1	0	12.2	
		4	-69.1	1	0	21.7	
	78BrErLy ³²	0	-72.6	9	5	77.0	
		1	-137.5	6	3	123.1	
		2	-28.5	22	12	24.2	
		91GrFa ³³	3	-26.7	17	13	39.5
		92HeCrJe ³⁴	3	-2.0	27	26	2.1
	97SpMeMe ³⁵	3	-40.5	20	4	11.7	
		0	-76.7	11	4	34.9	
1		-77.1	9	3	27.0		
2		-87.2	23	0	33.0		
Theory	99PaYa ²⁸	3	-48.0	35	1	25.6	
		4	-15.3	21	12	6.1	

The columns are as follows: Type = Experiment or Theory

Ref = Reference

v = Vibrational quantum number

$\langle\Delta\% \rangle$ = Average percentage difference

Number = number of J resolved levels

C_A = Number of levels whose lifetimes agree within uncertainty

$\langle^R\Delta\% \rangle$: Average $^R\Delta\%$ for values which do not agree within uncertainty

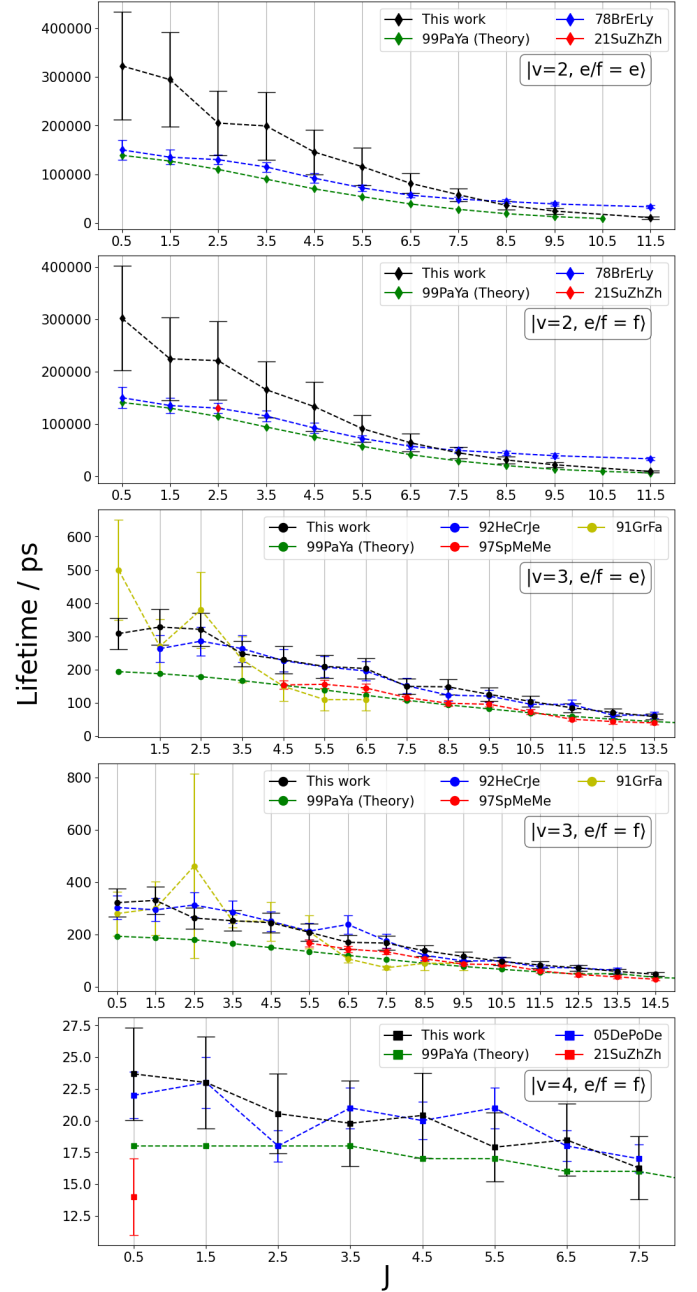


FIG. 10. Predissociation lifetimes as calculated in this work compared to experimental values from 05DePoDe³¹, 78BrErLy³², 91GrFa³³, 92HeCrJe³⁴, 97SpMeMe³⁵, and 21SuZhZh³⁶, and theoretical values from 99PaYa²⁸.

A visualisation of the computed predissociation lifetimes from this work against total angular momentum J is presented in Fig. 11. For $\nu > 4$ we find that lifetimes behave less predictably, wherein they do not decrease monotonically. The cause of this has not yet been identified with certainty however we expect this to be due to the quasi-bound energy level falling outside of the main crossing region.

In $\nu = 6$ we see that the lifetime increases and then falls again at $J = 15.5$. OH has a high rotational constant of around 20 cm^{-1} and in the high J limit there is an induced rotational barrier. This modifies the potential and introduces a further source of predissociation. In this limit, it would be expected that this added source of predissociation would lower the lifetime. This type of predissociation is particularly dominant in AIH and warrants further study⁶⁴.

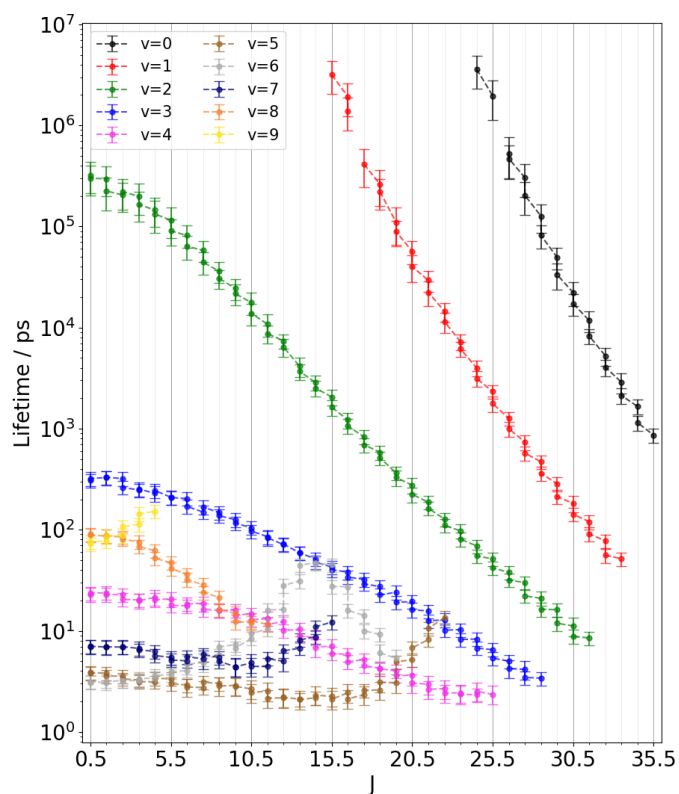


FIG. 11. Statistical predissociation lifetimes calculated for quasi-bound rovibronic $A \ ^2\Sigma^+$ state levels using code, BINSLT from Paper I. Lifetimes presented against J for varying ν

VI. CONCLUSION AND DISCUSSION

A spectroscopic model of OH from *ab initio* potential energy curves and coupling curves, and empirical coupling curves which are refined against latest empirical energies¹⁰ is produced using the nuclear motion code DUO. This spectroscopic model will be extended to include the $B \ ^2\Sigma^+$ and $C \ ^2\Sigma^+$ states, and combined with *ab initio* dipole moment curves to produce a line list and photoabsorption cross section for

hot OH as part of the ExoMol project. This line list will include predissociation lifetimes using the newly extended ExoMol data structure⁶⁵; broadening effects due to predissociation have been shown to be important in analyzing astronomical spectra.⁶⁴

424 quasi-bound $A \ ^2\Sigma^+$ state rovibronic levels are processed using the method of Paper I to calculate a set of 374 predissociation lifetimes, τ_p . This method has produced a set of predissociation lifetimes from first principles with uncertainties and provides a satisfactory level of agreement with experimental values. The method used in this paper allows for completeness over all levels considered in a spectroscopic model and is applicable to other systems.

According with the new ExoMol standards⁶⁶, predissociation lifetimes of molecules are to be included into the ExoMol line lists by convolution with the radiative lifetimes τ_r as in Eq. (22).

The non-zero contribution of the continuum $X \ ^2\Pi$ state levels to the line broadening of the $A \ ^2\Sigma^+$ state levels has been reported and shows that a predissociation into the continuum associated with the ground electronic state is of a small but non-zero probability. In this case, this contribution is negligibly small, however this may not be the case in all systems and warrants consideration in other predissociation studies. OH exhibits strong and complex predissociation dynamics through the interaction of three repulsive electronic states. It is, however, a streamlined example of this effect as the energetic limits of the repulsive states are the same as that of the ground state. This means that if one ignores asymptotic fine structure effects, the dissociation products are independent of the dissociation channel. As this method is generally applicable, molecules with more varied predissociation channels may be of interest for future branching ratio and lifetime studies.

SUPPLEMENTARY MATERIAL

The calculated predissociation lifetimes, a comparison with literature data, and the DUO input file are provided as supplementary material,

ACKNOWLEDGEMENTS

This work was supported by the European Research Council (ERC) under the European Union's Horizon 2020 research and innovation programme through Advance Grant number 883830 and the UK STFC under grant ST/R000476/1. The authors acknowledge the use of the UCL Myriad High Performance Computing Facility (Myriad UCL), and associated support services, in the completion of this work

DATA AVAILABILITY

All data is included in the main manuscript or as Supplementary Material. The full lifetime calculation code, BINSALT, is freely available at [ExoMol GitHub](#).

REFERENCES

- ¹G. Sun, X.-F. Zheng, Y. Qin, Y. Song, J. Zhang, J. M. Amero, and G. J. Vázquez, *Chinese J. Chem. Phys.* **33**, 129 (2020).
- ²W. Zhou, Y. Yuan, and J. Zhang, *J. Chem. Phys.* **119**, 9989 (2003).
- ³D. C. Radenović, A. J. van Rooij, S.-M. Wu, J. T. Meulen, D. H. Parker, M. P. van der Loo, L. M. Janssen, and G. C. Groenenboom, *Mol. Phys.* **106**, 557 (2008).
- ⁴J. B. Nee and L. C. Lee, *J. Chem. Phys.* **81**, 31 (1984).
- ⁵J. A. Joens, *J. Phys. Chem. A* **105**, 11041 (2001).
- ⁶R. G. Prinn, R. F. Weiss, B. R. Miller, J. Huang, F. N. Alyea, D. M. Cunnold, P. J. Fraser, D. E. Hartley, and P. G. Simmonds, *Science* **269**, 187 (1995).
- ⁷J. S. A. Brooke, P. F. Bernath, C. M. Western, C. Sneden, M. Afsar, G. Li, and I. E. Gordon, *J. Quant. Spectrosc. Radiat. Transf.* **138**, 142 (2016).
- ⁸R. Landman, A. Sanchez-Lopez, P. Molliere, A. Y. Kesseli, A. J. Louca, and I. A. G. Snellen, *Astron. Astrophys.* **656**, A119 (2021).
- ⁹S. O. M. Wright, S. K. Nugroho, M. Brogi, N. P. Gibson, E. J. W. de Mooij, I. Waldmann, J. Tennyson, H. Kawahara, M. Kuzuhara, T. Hirano, T. Kotani, Y. Kawashima, K. Masuda, J. L. Birkby, C. A. Watson, M. Tamura, K. Zwintz, H. Harakawa, T. Kudo, K. Hodapp, S. Jacobson, M. Konishi, T. Kurokawa, J. Nishikawa, M. Omiya, T. Serizawa, A. Ueda, S. Vievard, and S. N. Yurchenko, *Astron. J.* **166**, 41 (2023).
- ¹⁰T. Furtenbacher, S. T. Hegedus, J. Tennyson, and A. G. Császár, *Phys. Chem. Chem. Phys.* **24**, 19287 (2022).
- ¹¹E. F. van Dishoeck and A. Dalgarno, *J. Chem. Phys.* **79**, 873 (1983).
- ¹²S. R. Langhoff, E. F. van Dishoeck, R. Wetmore, and A. Dalgarno, *J. Chem. Phys.* **77**, 1379 (1982).
- ¹³E. F. van Dishoeck, S. R. Langhoff, and A. Dalgarno, *J. Chem. Phys.* **78**, 4552 (1983).
- ¹⁴E. F. Van Dishoeck and A. Dalgarno, *Icarus* **59**, 305 (1984).
- ¹⁵C. W. Bauschlicher Jr. and S. R. Langhoff, *J. Chem. Phys.* **87**, 4665 (1987).
- ¹⁶D. R. Yarkony, *J. Chem. Phys.* **97**, 1838 (1992).
- ¹⁷S. Lee and K. F. Freed, *J. Chem. Phys.* **87**, 5772 (1987).
- ¹⁸C. Kalyanaraman and N. Sathyamurthy, *Chem. Phys.* **187**, 219 (1994).
- ¹⁹S. Lee, *Chem. Phys. Lett.* **240**, 595 (1995).
- ²⁰S. Lee, *J. Chem. Phys.* **103**, 3501 (1995).
- ²¹S. Lee, *Chem. Phys. Lett.* **243**, 250 (1995).
- ²²S. Lee, *J. Phys. Chem.* **99**, 13380 (1995).
- ²³S. Lee, *J. Chem. Phys.* **104**, 1912 (1996).
- ²⁴E. F. van Dishoeck, M. C. van Hemert, A. C. Allison, and A. Dalgarno, *J. Chem. Phys.* **81**, 5709 (1984).
- ²⁵M. P. J. van der Loo and G. C. Groenenboom, *J. Chem. Phys.* **123**, 074310 (2005).
- ²⁶S. Srivastava and N. Sathyamurthy, *J. Phys. Chem. A* **118**, 6343 (2014).
- ²⁷X. Qin and S. D. Zhang, *J. Korean. Phys. Soc.* **65**, 2017 (2014).
- ²⁸G. Parlant and D. R. Yarkony, *J. Chem. Phys.* **110**, 363 (1999).
- ²⁹J. Tennyson, L. Lodi, L. K. McKemmish, and S. N. Yurchenko, *J. Phys. B: At. Mol. Opt. Phys.* **49**, 102001 (2016).
- ³⁰P. L. Raston, T. Liang, and G. E. Douberly, *J. Phys. Chem. A* **117**, 8103 (2013).
- ³¹E. L. Derro, I. B. Pollack, L. P. Dempsey, M. E. Greenslade, Y. Lei, D. Č. Radenović, and M. I. Lester, *J. Chem. Phys.* **122**, 244313 (2005).
- ³²J. Brzozowski, P. Erman, and M. Lyyra, *Phys. Scr.* **17**, 507 (1978).
- ³³J. A. Gray and R. L. Farrow, *J. Chem. Phys.* **95**, 7054 (1991).
- ³⁴D. E. Heard, D. R. Crosley, J. B. Jeffries, G. P. Smith, and A. Hirano, *J. Chem. Phys.* **96**, 4366 (1992).
- ³⁵J. J. L. Spaanjaars, J. J. ter Meulen, and G. Meijer, *J. Chem. Phys.* **107**, 2242 (1997).
- ³⁶G. Sun, W. Zhou, X. Zheng, Y. Qin, Y. Song, Y. Yuan, and J. Zhang, *Mol. Phys.* **119**, e1837974 (2021).
- ³⁷Y. Li and P.-Y. Zhang, *J. Theor. Comp. Chem.* **10**, 747 (2011).
- ³⁸M. L. Sink, A. D. Bandrauk, and R. Lefebvre, *J. Chem. Phys.* **73**, 4451 (2008).
- ³⁹S. N. Yurchenko, L. Lodi, J. Tennyson, and A. V. Stolyarov, *Comput. Phys. Commun.* **202**, 262 (2016).
- ⁴⁰G. B. Mitev, R. P. Brady, O. Smola, J. Tennyson, and S. N. Yurchenko, *Phys. Chem. Chem. Phys.* (2024), in preparation.
- ⁴¹H. J. Werner, P. J. Knowles, R. Lindh, F. R. Manby, and M. Schütz, “MOLPRO, a package of ab initio programs,” (2010), see <http://www.molpro.net/>.
- ⁴²H.-J. Werner, P. J. Knowles, G. Knizia, F. R. Manby, and M. Schütz, *WIREs Comput. Mol. Sci.* **2**, 242 (2012).
- ⁴³H.-J. Werner, P. J. Knowles, F. R. Manby, J. A. Black, K. Doll, A. Hefelmann, D. Kats, A. Köhn, T. Korona, D. A. Kreplin, Q. Ma, T. F. Miller, A. Mitrushchenkov, K. A. Peterson, I. Polyak, G. Rauhut, and M. Sibaev, *The Journal of Chemical Physics* **152**, 144107 (2020).
- ⁴⁴H.-J. Werner and P. J. Knowles, *The Journal of Chemical Physics* **82**, 5053 (1985).
- ⁴⁵S. R. Langhoff and E. R. Davidson, *Int. J. Quant. Chem.* **8**, 61 (1974).
- ⁴⁶A. T. Patrascu, C. Hill, J. Tennyson, and S. N. Yurchenko, *J. Chem. Phys.* **141**, 144312 (2014).
- ⁴⁷S. N. Yurchenko, L. Lodi, J. Tennyson, and A. V. Stolyarov, *Comput. Phys. Commun.* **202**, 262 (2016).
- ⁴⁸R. J. Le Roy, *J. Quant. Spectrosc. Radiat. Transf.* **186**, 179 (2017).
- ⁴⁹A. A. Šurkus, R. J. Rakauskas, and A. B. Bolotin, *Chem. Phys. Lett.* **105**, 291 (1984).
- ⁵⁰G. B. Mitev, S. Taylor, J. Tennyson, S. N. Yurchenko, A. A. Buchachenko, and A. V. Stolyarov, *MNRAS* **511**, 2349 (2022), <https://academic.oup.com/mnras/article-pdf/511/2/2349/42503999/stab3357.pdf>.
- ⁵¹M. Meuwly and J. M. Hutson, *J. Chem. Phys.* **110**, 8338 (1999).
- ⁵²S. Skokov, K. A. Peterson, and J. M. Bowman, *Chem. Phys. Lett.* **312**, 494 (1999).
- ⁵³A. Kramida, Y. Ralchenko, J. Reader, and NIST ASD Team, NIST Atomic Spectra Database (ver. 5.9), [Online]. Available: <http://physics.nist.gov/asd> [2021, October 31]. National Institute of Standards and Technology, Gaithersburg, MD. (2021).
- ⁵⁴G. Herzberg, in *Spectra of diatomic molecules* (Krieger Publ, 1989) pp. 223,257.
- ⁵⁵T. Rivlin, L. K. McKemmish, K. E. Spinlove, and J. Tennyson, *Mol. Phys.* **117**, 3158 (2019).
- ⁵⁶M. Pezzella, S. N. Yurchenko, and J. Tennyson, *Phys. Chem. Chem. Phys.* **23**, 16390 (2021).
- ⁵⁷A. U. Hazi and H. S. Taylor, *Phys. Rev. A* **1**, 1109 (1970).
- ⁵⁸V. A. Mandelshtam, T. R. Ravuri, and H. S. Taylor, *Phys. Rev. Lett.* **70**, 1932 (1993).
- ⁵⁹Z. Bacic and J. Simons, *The Journal of Physical Chemistry* **86**, 1192 (1982).
- ⁶⁰D. T. Colbert and W. H. Miller, *J. Chem. Phys.* **96**, 1982 (1992).
- ⁶¹J. Brown, A.-C. Cheung, and A. Merer, *Journal of Molecular Spectroscopy* **124**, 464 (1987).
- ⁶²R. J. Le Roy and Y. Huang, *Journal of Molecular Structure: THEOCHEM* **591**, 175 (2002).
- ⁶³R. J. Le Roy, *J. Quant. Spectrosc. Radiat. Transf.* **186**, 167 (2017).
- ⁶⁴Y. Pavlenko, J. Tennyson, S. N. Yurchenko, H. R. A. Jones, Y. Lyubchik, and A. Suárez Mascareño, *Mon. Not. R. Astron. Soc.* **516**, 5655 (2022).
- ⁶⁵J. Zhang, J. Tennyson, and S. N. Yurchenko, *RAS Tech. Instr.* (2024).
- ⁶⁶J. Tennyson, M. Pezzella, J. Zhang, and S. N. Yurchenko, *RAS Tech. Instr.* **2**, 231 (2023).